

CO-dark gas and molecular filaments in Milky Way-type galaxies – II: The temperature distribution of the gas

Simon C. O. Glover¹ & Rowan J. Smith²

¹*Universität Heidelberg, Zentrum für Astronomie, Institut für Theoretische Astrophysik, Albert-Ueberle-Straße 2, 69120 Heidelberg, Germany*

²*Jodrell Bank Centre for Astrophysics, School of Physics and Astronomy, University of Manchester, Oxford Road, Manchester, M13 9PL, UK*

7 September 2021

ABSTRACT

We investigate the temperature distribution of CO-dark molecular hydrogen (H_2) in a series of disk galaxies simulated using the AREPO moving-mesh code. In conditions similar to those in the Milky Way, we find that H_2 has a flat temperature distribution ranging from 10–100 K. At $T < 30$ K, the gas is almost fully molecular and has a high CO content, whereas at $T > 30$ K, the H_2 fraction spans a broader range and the CO content is small, allowing us to classify gas in these two regimes as CO-bright and CO-dark, respectively. The mean sound speed in the CO-dark H_2 is $c_{\text{s, dark}} = 0.64 \text{ km s}^{-1}$, significantly lower than the value in the cold atomic gas ($c_{\text{s, cnm}} = 1.15 \text{ km s}^{-1}$), implying that the CO-dark molecular phase is more susceptible to turbulent compression and gravitational collapse than its atomic counterpart. We further show that the temperature of the CO-dark H_2 is highly sensitive to the strength of the interstellar radiation field, but that conditions in the CO-bright H_2 remain largely unchanged. Finally, we examine the usefulness of the [C II] and [O I] fine structure lines as tracers of the CO-dark gas. We show that in Milky Way-like conditions, diffuse [C II] emission from this gas should be detectable. However, it is a problematic tracer of this gas, as there is only a weak correlation between the brightness of the emission and the H_2 surface density. The situation is even worse for the [O I] line, which shows no correlation with the H_2 surface density.

Key words: astrochemistry – hydrodynamics – ISM: clouds – ISM: molecules – galaxies: ISM

1 INTRODUCTION

Star formation within our Galaxy appears to occur exclusively within clouds of molecular gas. It is therefore important to understand the physical conditions within these clouds if we want to understand the role they play in star formation. Ideally, we would do this by studying the line emission from molecular hydrogen (H_2), which is by far the most abundant molecule within these clouds. Unfortunately, however, the temperature within the bulk of these clouds is too low to excite even the lowest accessible rotational transition of H_2 , meaning that H_2 emission is useful only for tracing atypical regions such as the shock fronts created by protostellar outflows (see e.g. Reipurth & Bally 2001). Consequently, if we want to learn about the physical conditions within the clouds (temperatures, densities, velocity structure, etc.), we have to rely on information provided by other observational tracers.

The most widely used tracer molecule is carbon monox-

ide (CO). This is the second most abundant molecular species within typical molecular clouds and its lowest rotational transitions are easily excited at the gas temperatures found there. Observations of CO line emission have therefore become one of the main ways in which we study the properties of both Galactic and extragalactic molecular clouds (see e.g. Jackson et al. 2006; Hughes et al. 2013). However, chemical modelling of clouds has long made clear that CO is not a perfect tracer of H_2 (see e.g. Tielens & Hollenbach 1985; van Dishoeck & Black 1988). H_2 is far more effective than CO at shielding itself against the effects of ultraviolet photodissociation, and as a result the transition from atomic to molecular hydrogen within a cloud illuminated by the interstellar radiation field (ISRF) does not necessarily occur in the same location as the transition from C^+ to C to CO. Consequently, observations of CO alone miss a significant fraction of the H_2 .

This CO-poor or “CO-dark” molecular gas has at-

arXiv:1607.08253v1 [astro-ph.GA] 27 Jul 2016

tracted increasing interest in the past few years, prompted by the realization that it may represent a significant fraction of the total molecular gas budget of the Milky Way. Observations (Grenier et al. 2005; Allen et al. 2012; Paradis et al. 2012; Langer et al. 2014) and theoretical studies (Wolfire et al. 2010; Smith et al. 2014) suggest that in conditions typical of the local ISM, anywhere between 30% and 70% of the total mass of H_2 may be located in regions that are CO-poor and that are hence not traced by observations of CO emission.

Observational constraints on the temperature distribution of the molecular gas in the ISM primarily come from observations of molecules such as CO itself or ammonia (NH_3) that are only found in large quantities within CO-rich gas. These observations therefore only constrain the temperature of the CO-rich molecular gas. The temperature distribution in the CO-dark phase is much harder to constrain observationally. In cases where there is a bright ultraviolet (UV) background source (e.g. an AGN), H_2 can be observed in absorption via its Lyman-Werner band transitions, allowing one to constrain its temperature, but these observations only probe gas in a very small fraction of the ISM (see e.g. Rachford et al. 2009). Since the CO-dark gas is much less well-shielded against the effects of the ISRF than the CO-rich gas, there are good reasons for believing that its temperature distribution could be significantly different from that in the CO-rich regions, an assumption which seems to be borne out by the high ($T \sim 50\text{--}100$ K) H_2 temperatures recovered from UV absorption line studies. If the temperature of the CO-dark gas does significantly differ from that of the CO-rich gas, then this is important as the temperature of the gas controls its sound-speed, and hence influences its stability against gravitational collapse as well as its response to the effects of supersonic turbulence (Padoan et al. 1997; Molina et al. 2012). The temperature of the molecular gas also affects the rate at which chemical reactions take place within it and so is an important input into any chemical model of the CO-dark molecular phase. Finally, the temperature of the CO-dark molecular gas also strongly influences the ease with which it can be detected using the atomic fine structure transitions of ionized carbon (C^+) and atomic oxygen (O).

In an effort to better understand the properties of the CO-dark molecular gas in galaxies like our own Milky Way, we have carried out detailed hydrodynamical simulations of a representative portion of the disk of a massive spiral galaxy (Smith et al. 2014). These simulations combine a state-of-the-art hydrodynamical code with a detailed treatment of the small-scale cooling physics and chemistry, and allow us to study the properties of the molecular phase in unprecedented detail. In this paper, we study in detail the temperature distribution of the molecular gas in these simulations, and assess its detectability using the fine structure lines of C^+ and O.

The structure of our paper is as follows. In Section 2, we briefly summarize the numerical method used for our simulations and the initial conditions that we adopt. (A more lengthy discussion of both can be found in Smith et al. 2014). In Section 3, we investigate the temperature distribution of the H_2 in our fiducial ‘‘Milky Way’’ simulation, and show that the temperatures that we derive for the CO-dark molecular component are in good agreement with previous

theoretical predictions. In Section 4, we extend the scope of our study to our other three simulations, allowing us to assess the effect of changing the mean gas surface density and the strength of the interstellar radiation field. In Section 5, we use a simple approximation to estimate the surface brightness of our simulated galaxies in the [C II] $158\ \mu\text{m}$, [O I] $63\ \mu\text{m}$ and [O I] $145\ \mu\text{m}$ fine structure lines and investigate how well the emission in these lines traces the CO-dark molecular gas. We discuss our results in Section 6 (including a discussion of some possible caveats) and present our conclusions in Section 7.

2 SIMULATIONS

2.1 Numerical approach

The galactic disk simulations analyzed in this paper are the same as those presented in Smith et al. (2014), and so we give only a brief description here and refer interested readers to that paper for more details. The simulations were carried out using a modified version of the AREPO moving-mesh code (Springel 2010). AREPO is a novel hydrodynamical code that solves the fluid equations on an unstructured mesh, defined as the Voronoi tessellation of a set of mesh-generating points that can move freely with the gas flow. It combines many of the strengths of modern Eulerian hydrodynamical codes with those of smoothed particle hydrodynamics, and has been successfully applied to problems ranging from the formation of the first stars (Greif et al. 2011, 2012) to the dynamical evolution of clouds close to the Galactic Centre (Bertram et al. 2015).

We have modified AREPO to add a simplified treatment of the chemistry of the ISM, as discussed in detail in Smith et al. (2014). We model the chemistry of hydrogen using the same treatment as in Glover & Mac Low (2007a,b), and model the formation and destruction of CO using the approximate model introduced by Nelson & Langer (1997). The radiative heating and cooling of the gas is treated using the detailed atomic and molecular cooling function introduced in Glover et al. (2010) and updated in Glover & Clark (2012a).

To model the attenuation of the interstellar radiation field due to H_2 self-shielding, CO self-shielding, the shielding of CO by H_2 , and by dust absorption, we use the TREECOL algorithm (Clark, Glover & Klessen 2012). This algorithm allows us to calculate a 4π steradian map of the dust extinction and the column densities of H_2 and CO surrounding each AREPO cell in an approximate but computationally efficient fashion. The resulting maps consist of 48 equal-area pixels, constructed using the HEALPIX algorithm (Górski et al. 2005). The functions to convert from H_2 and CO column densities to the corresponding shielding factors were taken from Draine & Bertoldi (1996) and Lee et al. (1996), respectively. When constructing our column density and extinction maps, we include contributions only from gas at distances $L \leq 30$ pc from the cell of interest. This value is motivated by the fact that in the local ISM, the typical distance to the nearest UV-bright star is approximately 30 pc (Reed 2000; Maíz-Apellániz 2001).

We neglect the effects of self-gravity and stellar feedback. The lack of stellar feedback means that we will tend

to over-produce molecular clouds, although this is offset to some extent by the absence of self-gravity, which will decrease the number of large clouds formed (c.f. Girichidis et al. 2016). Note that absence of self-gravity is unlikely to be a major obstacle in forming H_2 , as the transition from H to H_2 typically occurs at number densities $n < 100 \text{ cm}^{-3}$, where the contribution from self-gravity remains small in comparison to the effects of the global potential.

2.2 Initial conditions

The initial setup of each simulation is a torus of thickness 200 pc, inner radius 5 kpc, and outer radius 10 kpc. We do not include the inner portion of the disc, both for reasons of computational efficiency, and also because the behaviour of gas in this region will be strongly influenced by interactions with the galactic bar, if one is present. An analytical gravitational potential is applied to the torus to represent the influence of the stellar component of the galaxy. This potential is taken from Dobbs, Bonnell & Pringle (2006) and combines a logarithmic potential producing a flat rotation curve with $v_{\text{rot}} = 220 \text{ km s}^{-1}$ (Binney & Tremaine 1987), a potential for the outer halo taken from Caldwell & Ostriker (1981), and a four-armed spiral component from Cox & Gómez (2002). The gas is initially in rotation at $v = v_{\text{rot}}$ and develops pronounced spiral structure as it passes through the spiral potential (see Figure 1).

As described in Smith et al. (2014), we perform four simulations with different gas surface densities and radiation field strengths (see Table 1). Our fiducial “Milky Way” model has an initial gas surface density $\Sigma = 10 \text{ M}_{\odot} \text{ pc}^{-2}$ and a radiation field strength given by Draine (1978). In addition, we explore the effects of decreasing the surface density while either keeping the radiation field strength fixed (the Low Density model) or also decreasing it (the Low & Weak model). Finally, we also ran one simulation in which $\Sigma = 10 \text{ M}_{\odot} \text{ pc}^{-2}$ but the radiation field strength was increased by a factor of ten (the Strong Field model). We note that our assumption that the unattenuated radiation field strength is constant in both space and time is at best a crude approximation to the behaviour of the real ISM. However, Parravano, Hollenbach & McKee (2003) have shown that away from regions of massive star formation, the variations in the radiation field strength in representative patches of the diffuse ISM are relatively small, around a factor of a few. Therefore our “Milky Way” and “Strong Field” simulations should bracket the behaviour of the real Milky Way ISM for the range of Galactocentric radii modelled in our simulations.

In all of our simulations, the gas was taken to have solar metallicity, with a carbon abundance¹ $x_{\text{C,tot}} = 1.4 \times 10^{-4}$ and an oxygen abundance $x_{\text{O,tot}} = 3.2 \times 10^{-4}$ (Sembach et al. 2000). We assumed that the hydrogen and oxygen were initially in neutral atomic form, and that the carbon was present in the form of C^+ , as in unshielded gas it is easily ionized by the ISRF. The cosmic ray ionization rate

Table 1. Simulation parameters

Simulation	Surface Density ($\text{M}_{\odot} \text{ pc}^{-2}$)	Radiation Field Strength (relative to Draine 1978)
Milky Way	10	1
Low Density	4	1
Strong Field	10	10
Low & Weak	4	0.1

of atomic hydrogen was set to $\zeta_{\text{H}} = 3 \times 10^{-17} \text{ s}^{-1}$ in all four simulations (van der Tak & van Dishoeck 2000).

To achieve the resolution necessary for accurately following the formation of H_2 and CO in the ISM, we make use of the system of mass refinement present in AREPO. We focus our attention on a section of the disk, and simulate this section with an AREPO cell mass of 4 M_{\odot} . In most of the remainder of the disk, we adopt a much larger cell mass of 1000 M_{\odot} for reasons of computational efficiency. Between the high and low resolution regions, we have buffer zones in which we smoothly change the cell mass between 4 M_{\odot} and 1000 M_{\odot} . Because we keep the cell mass constant, our spatial resolution varies as a function of the local gas density. At the mean density of a typical GMC, it is significantly less than a parsec in our high resolution region. This high spatial resolution allows us to begin to resolve the dense filaments and cores that contain most of the CO, and also means that the dense molecular clouds that form in our simulations are generally resolved with thousands or tens of thousands of AREPO cells.

3 MOLECULAR GAS IN THE MILKY WAY SIMULATION

3.1 Temperature distribution as a function of chemical composition

We begin our study by examining the temperature distribution of the gas in our Milky Way simulation at a time $t = 261.1 \text{ Myr}$ after the beginning of the simulation. This time corresponds to one and a half complete rotations of our gas torus, which means that the gas has undergone six spiral arm passages. By this stage in the simulation, it has developed a considerable amount of dense, filamentary substructure, as illustrated in Figure 1. Moreover, since this time is orders of magnitude longer than the cooling time in the dense ISM, we can be confident that most of the gas has reached thermal equilibrium.

Figure 2a shows a mass-weighted histogram of the temperatures that we find in the gas. We see that the distribution is strongly bimodal: there is a pronounced peak at $T \sim 8000 \text{ K}$, corresponding to the temperature below which Lyman- α cooling becomes ineffective and a second, more extended peak around 100 K. The high temperature peak is dominated by atomic gas (see Figure 2b) and is easily identifiable as the warm neutral medium (WNM). The low temperature peak, on the other hand, consists of a mix of atomic gas (the cold neutral medium or CNM) and molecular gas. The absence of a hot phase with $T \gg 10^4 \text{ K}$ is a consequence of our neglect of stellar feedback in these simulations. The absence of feedback also means that there is less

¹ Unless otherwise noted, all fractional abundances quoted in this paper are measured with respect to the total number of hydrogen nuclei.

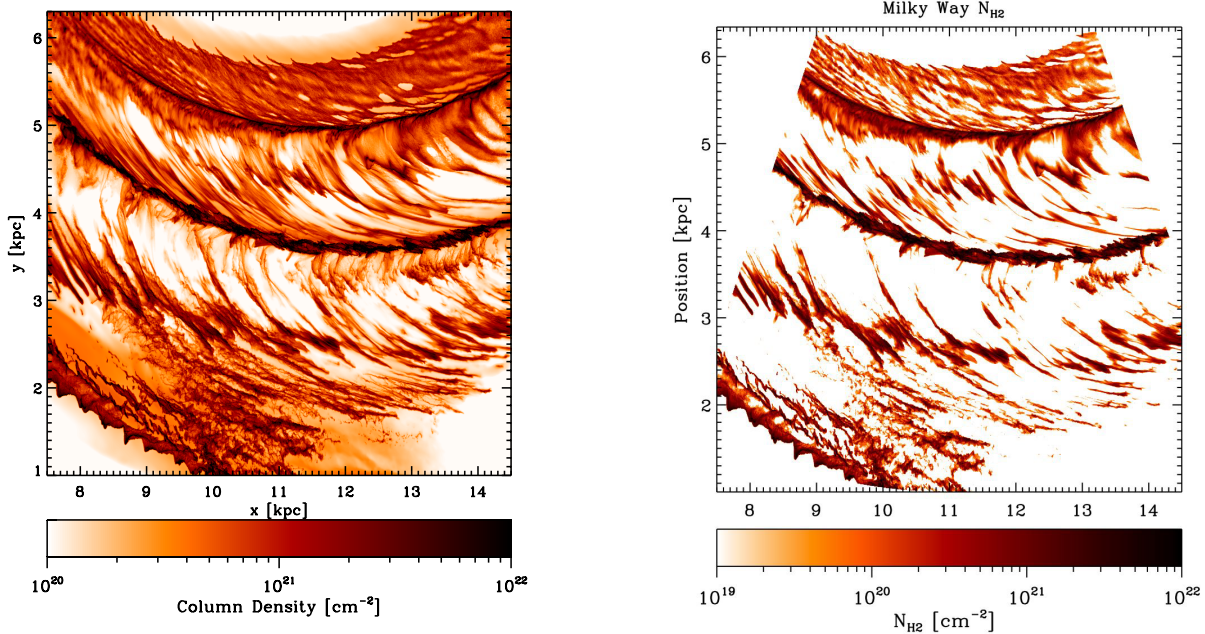


Figure 1. Left: map of total column density of hydrogen nuclei in a region centered on the highly-resolved section of the disc in the Milky Way simulation. Right: map of H_2 column densities for the same simulation. In this panel, we only show the gas within the highly-resolved region, as we do not properly resolve H_2 formation in the remainder of the disc. In both panels, the coordinate axes show the x and y positions of the gas within the simulation volume, with respect to an origin which we arbitrarily take to be at the bottom left of the volume.

mixing of material between the cold and warm phases, and hence less gas at intermediate temperatures than found in simulations that include supernova feedback (c.f. Hill et al. 2012; Gent et al. 2013; Walch et al. 2015; Hennebelle & Iffrig 2014).

Figure 2b shows how the temperature distribution changes if we weight by the mass of atomic hydrogen rather than by the total mass. At temperatures above a few hundred K, the gas is almost entirely atomic and so the temperature distribution is very similar to the one we recover when we weight by the total gas mass. At lower temperatures, however, there are clear differences between the two distributions. In both cases, there is a clear peak around $T \sim 100$ K, corresponding to the equilibrium temperature in the CNM, but there is much less gas at $T \ll 100$ K in the H-weighted distribution than in the distribution weighted by total gas mass. Figure 2c, which shows an H_2 mass-weighted histogram of the temperature, demonstrates that this difference in behaviour is due to a change in the chemical composition of the gas. Very little of the H_2 in the simulation is located in gas with $T > 100$ K, but at lower temperatures, a significant fraction of the gas is molecular.

Interestingly, Figure 2c shows that the temperature distribution of the H_2 is relatively flat in the temperature range between $10 < T < 100$ K, with comparable amounts of H_2 being found close to 10 K and close to 100 K.² This contrasts

² It is possible that this flat distribution results from two broad, overlapping peaks of roughly equal height, similar to the peaks of unequal height we find in our Strong field simulation (Section 4), but confirming this would require us to run additional simulations. In any case, whether the distribution is truly flat or

strikingly with what we find if we instead weight the temperature distribution by the mass of CO, rather than the H_2 mass (Figure 2d). The CO mass-weighted histogram shows a much narrower, strongly peaked temperature distribution centered around $T \sim 12$ K. Very little of the CO is located in regions with $T > 30$ K. This is consistent with observational determinations of the CO excitation temperature in typical Galactic GMCs, which recover values of around 10–30 K in regions not directly affected by stellar feedback (e.g. Roman-Duval et al. 2010; Polychroni, Moore & Allsopp 2012; Nishimura et al. 2015), although we caution that this only provides an accurate measure of the kinetic temperature if the CO emission is thermalized. Comparison of Figure 2c and Figure 2d therefore clearly demonstrates that in addition to the expected CO-bright molecular gas, which we can loosely identify as the H_2 with $10 < T < 30$ K, there is also a CO-dark molecular component with $T > 30$ K that contains a significant fraction of the total molecular gas mass, consistent with the results presented in Smith et al. (2014).

To help us to better characterize the nature of the gas in which we find H_2 but little or no CO, we have constructed a two-dimensional probability distribution function (PDF) for the H_2 fractional abundance and the gas temperature, weighted by the density of the gas. This is shown in Figure 3. We see from this Figure that the cold H_2 (i.e. the gas with $T < 30$ K) is almost all located in regions dominated by molecular hydrogen, and that this gas generally has a density $n > 100 \text{ cm}^{-3}$. On the other hand, the warmer H_2 (i.e.

broad and bimodal does not significantly affect our analysis or conclusions.

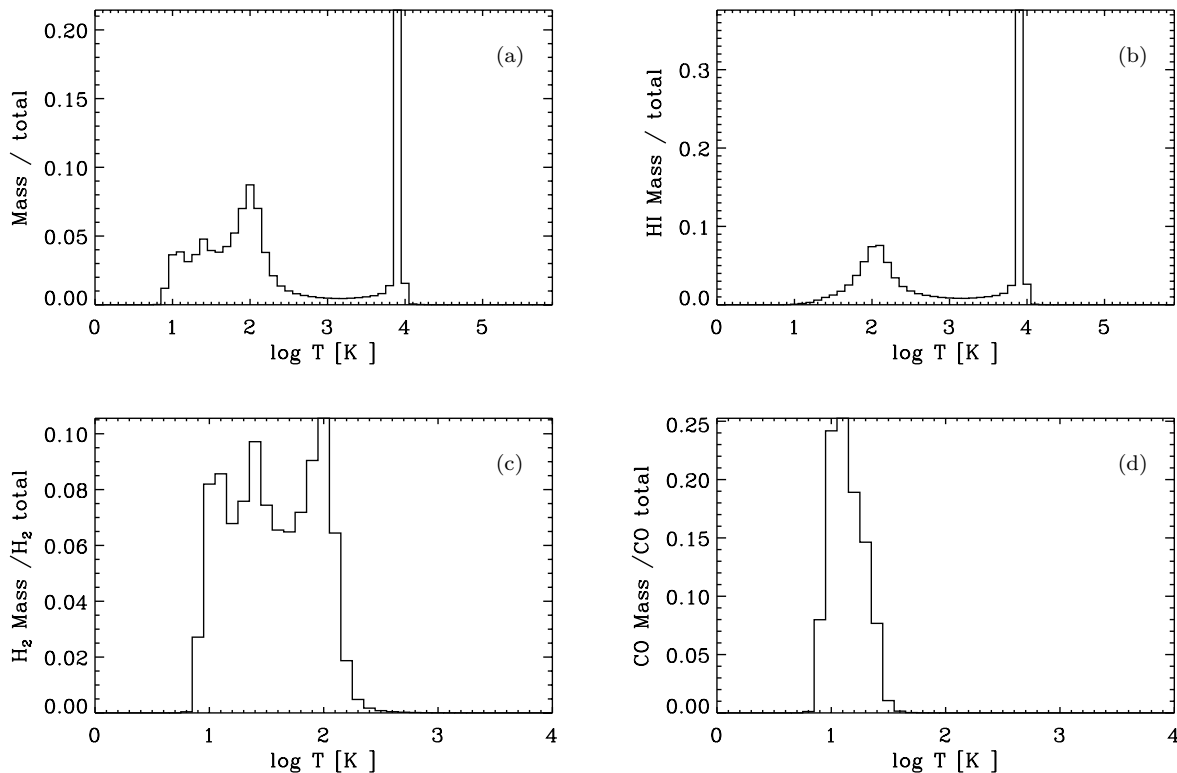


Figure 2. (a) Mass-weighted histogram of the gas temperature in our Milky Way simulation at time $t = 261.1$ Myr. The sharp peak just below 10^4 K corresponds to the temperature at which Lyman- α cooling becomes ineffective. The absence of gas at higher temperatures is a consequence of the fact that our simulations do not include the effects of stellar feedback. (b) As (a), but weighted by the mass of atomic hydrogen. (c) As (a), but weighted by the mass of molecular hydrogen. (d) As (a), but weighted by the mass of CO.

the component with $30 < T < 100$ K) is found in regions spanning a wide range of different H_2 abundances, ranging from values as small as $x_{H_2} \sim 0.01$ to as large as $x_{H_2} \sim 0.5$. Figure 3 also shows us that the density of this gas is systematically lower than that of the colder, CO-bright gas, typically lying in the range $10 < n < 100 \text{ cm}^{-3}$. This range of densities corresponds more closely to those expected in the atomic CNM than those found in molecular clouds. This plot therefore helps to emphasize the fact that the physical conditions in the CO-dark molecular gas differ significantly from those in the CO-rich regions: the CO-dark gas is systematically warmer and less dense than the CO-rich gas, and so observational probes of the temperature and density of the latter component do not give a good description of the behaviour of the CO-dark gas.

3.2 Comparison with previous numerical models

The range of temperatures that we find in the CO-dark gas in our Milky Way simulation is in good agreement with the results of previous theoretical models. For example, Wolfire et al. (2010) study the composition and properties of the CO-dark envelopes surrounding GMCs using a sophisticated 1D photodissociation region (PDR) code. They find that the bulk of the CO-dark gas in their models has a temperature in the range from 40–80 K. This is slightly narrower than the range we find in our simulation, but this may simply be

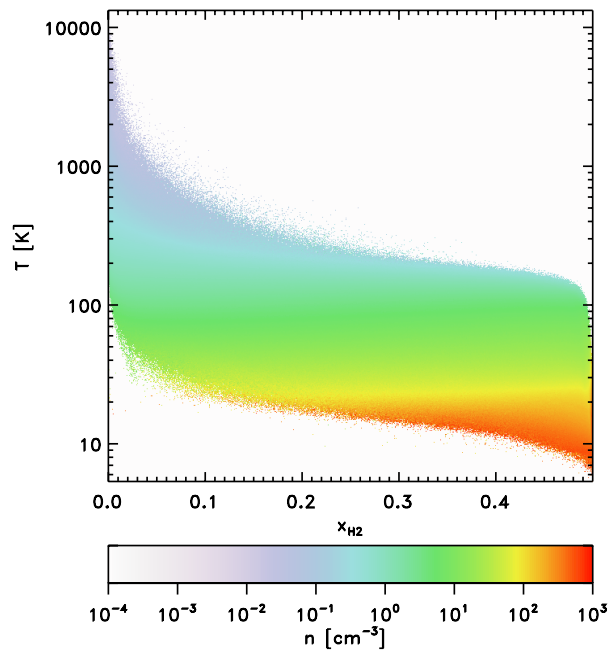


Figure 3. Two-dimensional density-weighted probability distribution function showing the H_2 fractional abundance and gas temperature in the Milky Way simulation at $t = 261.1$ Myr.

because their assumed densities are somewhat higher than the range of values that we find in our models. Wolfire et al. (2010) do not consider low extinction clouds that are not associated with bright CO emission, and so make no predictions for this case.

Another recent theoretical study of the chemical and thermal distribution of the gas within a representative CO-bright molecular cloud was carried out by Offner et al. (2013) using the three-dimensional PDR code 3D-PDR (Bisbas et al. 2012). They recover temperatures in the CO-dark component in the range 30–70 K. Again, they do not consider the case of a cloud without associated CO emission, and hence do not probe the full range of conditions in which we find CO-dark molecular gas.

In addition to these recent studies, there is also an extensive literature on the chemical and thermal modelling of diffuse molecular and translucent clouds (see e.g. the comprehensive review by Snow & McCall 2006). These clouds, observed in absorption, have large H₂ fractions but negligible CO, and hence represent part of the CO-dark molecular gas component in the ISM. Models of these clouds (e.g. Shaw et al. 2006) again recover characteristic temperatures in good agreement with those reported here.

Finally, dynamical models of the formation and evolution of individual molecular clouds that track the chemical and thermal evolution of the gas (e.g. Clark et al. 2012; Glover & Clark 2012b; Glover et al. 2015) can also be used to study the properties of the CO-dark molecular phase, yielding results that once again agree well with those from our Milky Way simulation.

An important point to note, however, is that although all of these models (including our own) show that the temperature of the CO-dark gas is sensitive to its density and extinction, most of the models are unable to predict the distributions of densities and extinctions within the gas, and hence are unable to predict how the gas is distributed within the 30–100 K temperature range that all of the models largely agree on. For example, in the PDR models, the density structure of the cloud is adopted as an input, rather than being an outcome of the modelling. The dynamical models discussed above do not suffer from this problem, as the temperature and density in these models are evolved together in a self-consistent fashion. However, in models that focus on individual clouds, there is always the concern that the results will be sensitive to the assumed initial conditions for the cloud. To avoid this problem, it is necessary to carry out dynamical simulations that evolve the ISM on scales much larger than the sizes of individual clouds, such as the disk models presented in this paper.

4 CHANGING THE SURFACE DENSITY AND RADIATION FIELD STRENGTH

In the previous section, we examined the temperature distribution of the molecular gas in our Milky Way simulation at a representative time during the evolution of the disk. In this section, we extend our analysis to consider the other three simulations originally presented in Smith et al. (2014): the Low Density, Strong Field, and Low & Weak simulations. Doing so allows us to investigate how the temperature distribution of the CO-dark molecular gas depends on the mean

surface density of the gas disk and the strength of the interstellar radiation field.

In the Low Density simulation, the H₂ mass-weighted temperature distribution is qualitatively different from the corresponding distribution in the Milky Way simulation. Instead of a relatively flat distribution of temperatures between 10 K and 100 K, we find that the distribution is sharply peaked around 100 K and falls off rapidly at both lower and higher temperatures. The high temperature fall off occurs for the same reason that it does in the Milky Way simulation: most of the gas with $T > 100$ K has a density $n < 10$ cm⁻³, and the equilibrium H₂ fraction in this low density part of the cold ISM is small. On the other hand, the fall off in the temperature distribution of the H₂ at low temperatures reflects the fact that only a small fraction of the gas in the low density disk is found in clouds that have surface densities high enough to shield themselves against the effects of photoelectric heating by the ISRF. This is consistent with our finding in Smith et al. (2014) that the dark gas fraction in this simulation is very high, $\sim 90\%$, since the extinction required to shield the gas effectively against CO photodissociation is similar to that required to shield it against photoelectric heating.

If we focus on the small fraction of gas that does develop a significant CO content by examining the CO mass-weighted temperature distribution (Figure 4b), then we see that in this case there is much less difference between the Low Density run and the Milky Way run: in both cases, the temperature distribution extends from around 10–30 K, with a peak in the middle of this range. This demonstrates that the thermodynamical condition of the gas within a CO-bright cloud is largely insensitive to the gas surface density of the galaxy averaged on much larger scales, which is a straightforward consequence of the fact that local gas and dust shielding dominates in these clouds.

If we now look at the temperature distribution of the H₂ in the Strong Field simulation (Figure 5a) we find that its behaviour lies in between that in the Milky Way simulation at that in the Low Density simulation. As in the Low Density simulation, the distribution is dominated by a peak close to $T \sim 100$ K, corresponding to CO-dark H₂ that is located in gas that is efficiently heated by the stronger ISRF. However, the temperature distribution does not fall off as rapidly as we move to lower temperatures as in the Low Density run, and there is a clear second peak at $T \sim 30$ K, corresponding to the H₂ located in CO-bright clouds. The CO-weighted temperature distribution is again narrow, with a single peak, but is shifted to higher temperatures compared to its value in the Milky Way simulation, peaking at around 30 K (see Figure 5b).

Finally, in the Low and Weak simulation, we find that the H₂ has a broad and multiply-peaked distribution of temperatures, similar to the behaviour in the Milky Way run. However, in this case, the main peak is located at low temperatures, $T \sim 25$ K, owing to the low photoelectric heating rate in this simulation. The CO temperature distribution is also shifted to lower values, peaking just below 10 K.

In summary, we see that the temperature distribution of the H₂ is highly sensitive to both the strength of the ISRF and also the mean surface density of the gas in the disk. Simulations with high values for the ISRF strength or low surface densities produce much more warm H₂ than

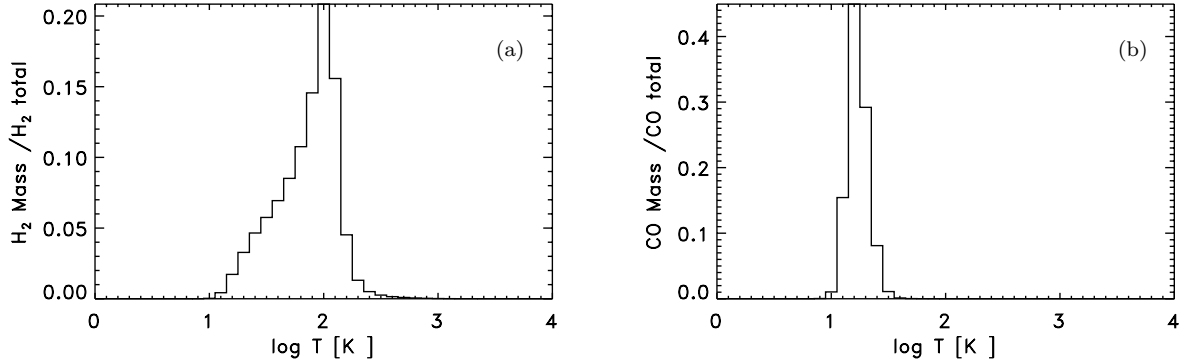


Figure 4. (a) Histogram of the gas temperature in our Low Density simulation at time $t = 261.1$ Myr, weighted by the H₂ mass. (b) As (a), but weighted by the mass of CO.

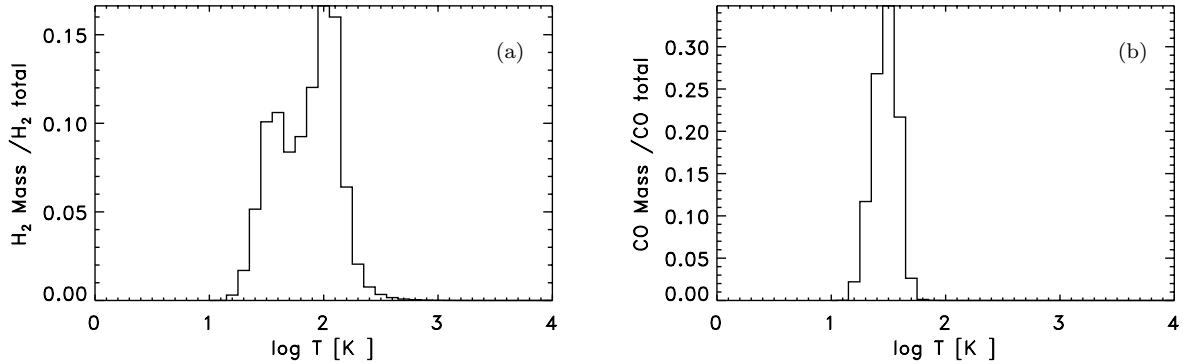


Figure 5. (a) Histogram of the gas temperature in our Strong Field simulation at time $t = 261.1$ Myr, weighted by the H₂ mass. (b) As (a), but weighted by the mass of CO.

cold H₂. On the other hand, the run with the canonical Milky Way values for these parameters yields an approximately flat H₂ temperature distribution, and the run with a low value for the ISRF strength produces a distribution that is dominated by cold H₂. The temperature distribution of CO in the simulations displays less variation, with all four runs producing a narrow distribution with a single peak. However, the location of this peak does vary if we change the strength of the ISRF, ranging from 8 K in the Low and Weak simulation to 33 K in the Strong Field simulation. This is consistent with the observations of molecular clouds presented in Roman-Duval et al. (2010) that show a systematic increase in the mean CO excitation temperature with decreasing Galactocentric radius (and hence increasing ISRF strength), although we caution that this might also reflect a change in the mean density of the clouds.

5 CAN WE MAP CO-DARK MOLECULAR GAS USING [C II] AND [O I]?

5.1 Generating maps of [C II] and [O I] emission

As we have seen in the previous sections, the characteristic temperature of CO-dark molecular gas is significantly higher than that of the CO-rich gas making up most GMCs.

This raises the prospect of detecting this CO-dark molecular component using the fine structure lines of ionized carbon and neutral oxygen.

The C⁺ ground state is split into two fine structure levels, ²P_{1/2} and ²P_{3/2}, separated by an energy $E_{10}/k = 92$ K, where k is Boltzmann’s constant. For O, we have instead three fine structure levels in the ground state, ³P₂, ³P₁ and ³P₀, with energy separations of $E_{10}/k = 227$ K between ³P₂ (the lowest energy level) and ³P₁ and $E_{20}/k = 327$ K between ³P₂ and ³P₀. At typical GMC temperatures of 10–30 K, it is difficult to excite any of the excited levels of C⁺ or O. For example, the exponential factor in the collisional excitation rate of C⁺ has a value of $e^{-9.2} \simeq 10^{-4}$ at 10 K and $e^{-9.2/3} \simeq 0.05$ at 30 K. Emission from the [O I] lines is suppressed even more strongly at these temperatures. However, at the higher temperatures found in the CO-dark molecular gas, the situation is more promising: at 60 K, for instance, the [C II] excitation rate is suppressed by a factor of only $e^{-9.2/6} \sim 0.2$.

For this reason, it is interesting to compute how bright the [O I] and [C II] emission from the CO-dark molecular component is likely to be, in order to allow us to assess how easy it will be to detect the CO-dark H₂ using these lines. The obvious way in which to do this would be to take the results of our simulation and run them through a full ra-

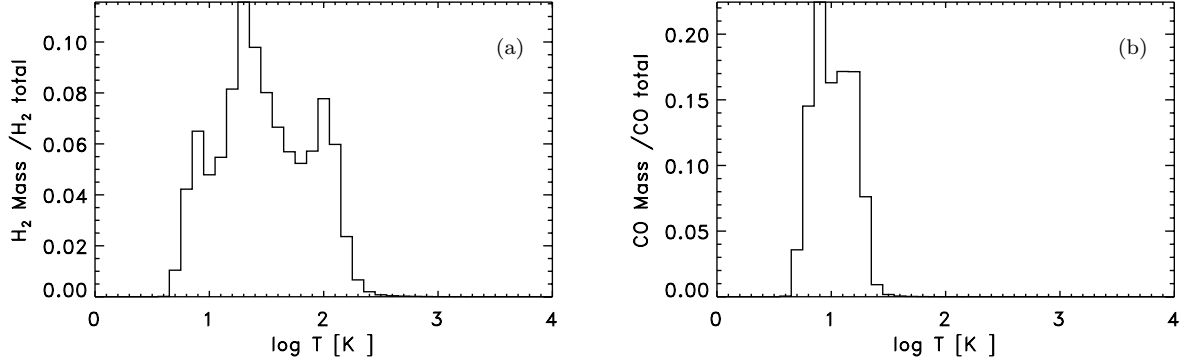


Figure 6. (a) Histogram of the gas temperature in our Low & Weak simulation at time $t = 261.1$ Myr, weighted by the H_2 mass. (b) As (a), but weighted by the mass of CO.

diative transfer code, as we have done with many of our smaller-scale simulations in previous papers (e.g. Smith et al. 2013; Glover et al. 2015). Unfortunately, the sheer size of the simulations studied in this paper renders this impractical: none of the line radiative transfer codes to which we have access can handle problems with hundreds of millions of discrete resolution elements and dynamical ranges that run from ~ 0.3 pc (the best spatial resolution we achieve in the highest resolution parts of the disk) up to a few kpc.

Fortunately, it is possible to get a reasonably good idea of the likely strength of the [C II] and [O I] emission without needing to solve the full radiative transfer problem, simply by assuming that the fine structure lines are optically thin. In this limit, we can calculate the total integrated brightness of the [C II] $158 \mu\text{m}$ line or the [O I] $63 \mu\text{m}$ and $145 \mu\text{m}$ lines along a given line of sight simply by summing up the total number of photons emitted in these lines in the direction of interest, without needing to worry about whether any of these photons are later absorbed. The conditions in which this assumption is likely to be valid are discussed in Appendix A.

Having made the assumption that the [C II] and [O I] lines are optically thin, we can compute the amount of energy radiated in each line per unit volume by assuming that the fine structure levels are in statistical equilibrium and solving the appropriate set of algebraic equations for the level populations. For example, in the case of [C II], if we denote the fractional population of the ground-state as x_0 and the fractional population of the excited state as x_1 , then

$$(A_{10} + B_{10}J_{10} + C_{10})x_0 = (B_{01}J_{10} + C_{01})x_1, \quad (1)$$

where A_{10} , B_{10} and B_{01} are the Einstein coefficients for spontaneous emission, stimulated emission and absorption for the $1 \rightarrow 0$ transition, respectively, J_{10} is the mean specific intensity of the incident radiation field at the wavelength of the line, and C_{01} and C_{10} are the collisional excitation and de-excitation rates, respectively. Since we also know that $x_0 + x_1 = 1$, it is simple to derive the following expression for x_1 :

$$x_1 = \frac{A_{10} + B_{10}J_{10} + C_{10}}{A_{10} + (B_{10} + B_{01})J_{10} + C_{10} + C_{01}}. \quad (2)$$

To solve this, we need to specify the various excitation and de-excitation rates, as well as the value of J_{10} . For A_{10} we

adopt the value $A_{10} = 2.3 \times 10^{-6} \text{s}^{-1}$ specified in the LAMDA database (Schöier et al. 2005); B_{01} and B_{10} then follow from this via the standard relationships. Our value for J_{10} is taken from Mathis et al. (1983). In our Milky Way simulation, we interpolate the value at $158 \mu\text{m}$ from their tabulated values for the field strength in the wavelength range $8\text{--}1000 \mu\text{m}$ for the solar neighbourhood (see their Table B1). For our other simulations, we assume that the field strength at this frequency scales linearly with the UV field strength – i.e. we adopt a value ten times larger in the Strong Field simulation and ten times weaker in the Low and Weak simulation. Since we expect the ISRF at $158 \mu\text{m}$ to be dominated by dust emission rather than by the CMB, this simple rescaling procedure is appropriate, at least at the level of accuracy of the calculations reported on here. For C_{10} , we account for collisions between C^+ and electrons, hydrogen atoms and H_2 molecules, using rate coefficients taken from Wilson & Bell (2002), Hollenbach & McKee (1989) and Wiesenfeld & Goldsmith (2014), respectively, and values for the number densities of e^- , H and H_2 taken from the simulations. Finally, C_{01} follows from C_{10} if we apply the principle of detailed balance.

Given x_1 , we can then compute the frequency-integrated emissivity for the [C II] line,

$$j_{\text{CII}} = \frac{1}{4\pi} (A_{10} + B_{10}J_{10}) E_{10} x_1 n_{\text{C}^+}, \quad (3)$$

where n_{C^+} is the number density of C^+ ions. However, as the AREPO cells do not have a fixed volume, in practice it is easier to work in terms of the emissivity per unit mass

$$\frac{j_{\text{CII}}}{\rho} = \frac{(A_{10} + B_{10}J_{10}) E_{10} x_1 n_{\text{C}^+}}{4\pi\rho}. \quad (4)$$

The procedure in the case of the two [O I] lines is very similar, except that in this case we have to solve three coupled linear equations for the fractional level populations of the ground state and the two excited states. As with [C II], we take the required atomic data from the LAMDA database. When computing the collisional excitation and de-excitation rates, we consider the effects of collisions with electrons, protons, atomic hydrogen and H_2 , using data from Bell, Berrington & Thomas (1998), Pequignot (1990), Abrahams-son, Krens & Dalgarno (2007) and Jaquet et al. (1992), re-

spectively. We also account for the effects of charge transfer with H^+



followed by the inverse process



This pair of reactions can leave the oxygen atom in a different fine structure state from the one that it started in, with the result that these reactions can in some cases significantly affect the oxygen fine structure level populations (Pequignot 1990). To model the effects of these reactions we make use of the fine-structure resolved rate coefficients for both processes computed by Stancil et al. (1999).

Finally, given the emissivity per unit mass for the $[\text{C II}]$ line for each AREPO cell, we can compute the total $[\text{C II}]$ emissivity for the cell simply by multiplying by the mass contained in the cell. The resulting distribution of emissivities can be analyzed directly, and we can also make maps of the emission by integrating along selected lines of sight. The same procedure can also be used for the two $[\text{O I}]$ lines.

It is important to note that because our simulations do not include star formation or stellar feedback, we are unable to model the $[\text{C II}]$ or $[\text{O I}]$ emission directly associated with regions of massive star formation. In reality, some of the $[\text{C II}]$ observed in real galaxies is produced within H II regions, and a further substantial fraction is produced within the bright PDRs surrounding massive O and B-type stars. These PDRs also generate much of the observed $[\text{O I}]$ emission. Our synthetic images do not account for these sources and this should be borne in mind when interpreting our results.

5.2 Analysis

5.2.1 Results from the Milky Way simulation

In Figure 7, we show how the estimated $[\text{C II}]$ emissivity is distributed as a function of density and temperature in the Milky Way simulation at time $t = 261.1$ Myr. The distribution with respect to number density is bimodal, with a small peak centered on $n \sim 0.2 \text{ cm}^{-3}$, corresponding to emission from the WNM, and a much larger peak at $n \sim 20 \text{ cm}^{-3}$, corresponding to emission from the cold atomic and CO-dark molecular gas. The distribution with respect to temperature tells us a similar story, with a sharp peak just below 10^4 K corresponding to the emission from the WNM and a broader peak around 100 K corresponding to emission from the cold atomic and molecular gas.

We saw in Section 3.1 that the temperature distribution of the H_2 in the Milky Way simulation is relatively flat between $T \sim 10$ K and $T \sim 100$ K. This is not the case with the $[\text{C II}]$ emissivity, which decreases sharply with decreasing temperature, owing to the influence of the $e^{-92/T}$ term in the collisional excitation rate. It is therefore clear that the $[\text{C II}]$ emission cannot be tracing all of the H_2 equally well. Indeed, if we compare the temperature distribution of the $[\text{C II}]$ emission with the CO mass-weighted temperature distribution shown in Figure 2d, we see that there is little overlap: $[\text{C II}]$ is a very poor tracer of the cold, dense CO-bright clouds, but performs much better as a tracer of warmer, more diffuse gas.

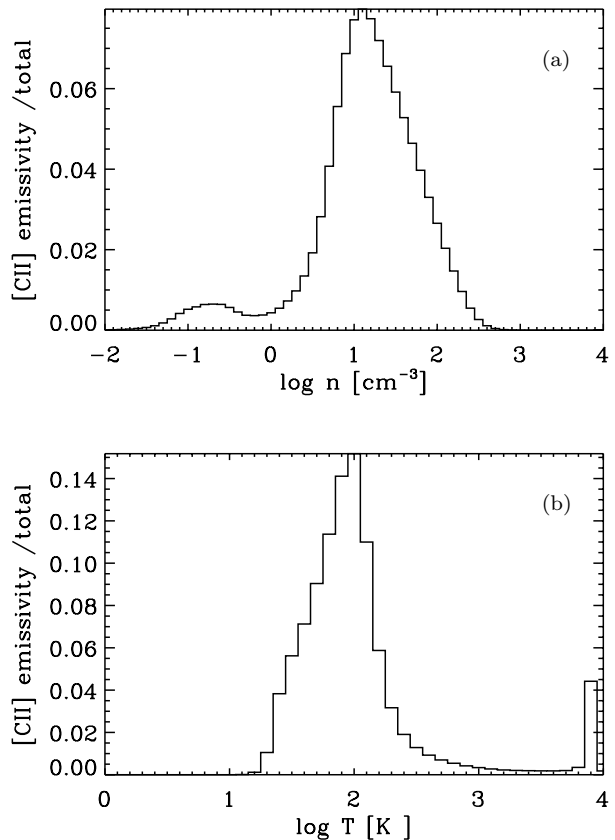


Figure 7. (a) Distribution of the estimated $[\text{C II}]$ emissivity as a function of the gas number density in our Milky Way simulation at time $t = 261.1$ Myr. (b) As (a), but showing the distribution with respect to the gas temperature.

There remains the question of how much of the total $[\text{C II}]$ emission in our simulations is produced by CO-dark molecular gas and how much comes instead from atomic gas. To address this, we have constructed a histogram of the $[\text{C II}]$ emissivity as a function of the fractional abundance of atomic hydrogen, shown in Figure 8. We see that there is a clear peak close to $x_{\text{H}} \sim 0$, corresponding to emission from gas which is almost entirely molecular. However, there is also substantial emission coming from regions with atomic hydrogen fractions significantly greater than zero. If we define H_2 -dominated regions to be those with $x_{\text{H}} < 0.5$ (i.e. with more than half of their total hydrogen in the form of H_2), and H-dominated regions to be those with $x_{\text{H}} \geq 0.5$, then we find that around half of the total $[\text{C II}]$ emission is produced in H_2 -dominated gas, while the other half is produced in H-dominated gas. For comparison, we note that Velusamy & Langer (2014) find that in our own Galaxy, the ratio of the total $[\text{C II}]$ emission produced by H_2 -dominated diffuse gas (i.e. by H_2 in regions which are not PDRs) to that produced by H-dominated gas is roughly 57% to 43%, in fairly good agreement with our results. However, at this point, it is worthwhile reminding the reader that our simulations do not account for the effects of stellar feedback. Our estimates of the $[\text{C II}]$ emission therefore do not account for the contributions coming from H II regions and the bright

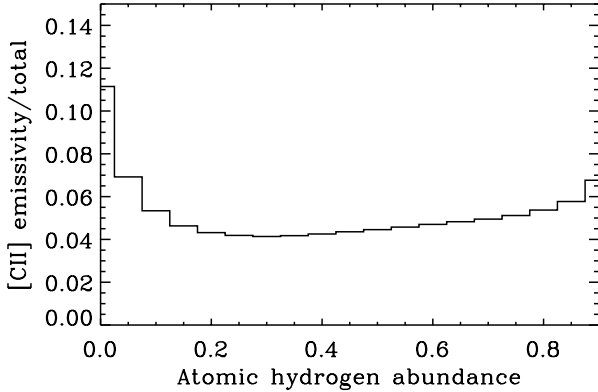


Figure 8. As Figure 7a, but showing the distribution of [C II] emissivity as a function of the fractional abundance of atomic hydrogen.

PDRs around massive O and B stars, which together are responsible for roughly 75% of the total [C II] emission of the Milky Way (Velusamy & Langer 2014). Our estimates of the relative fractions of the [C II] emission produced by H₂-dominated and H-dominated gas therefore only apply to the diffuse emission powered by the mean ISRF and not to the emission coming from these brighter regions.

It is also important to remind the reader that our estimate here assumes that [C II] remains optically thin. In practice, many of the lines of sight with the highest H₂ column densities lie in the regime where [C II] is likely to become optically thick (see Figure 9), and so it is possible that we are overestimating the [C II] emission from the highly molecular gas to some degree. Note, however, that even if the [C II] line is optically thick, if the gas density is much lower than the critical density for the transition, the [C II] line can be “effectively” optically thin (Goldsmith et al. 2012). In this case, the [C II] photons produced will scatter but most will eventually escape, and so in this regime the total [C II] luminosity is relatively insensitive to the [C II] optical depth. Goldsmith et al. (2012) show that for H₂-dominated gas, $n_{\text{cr}} = 6100 \text{ cm}^{-3}$ at 100 K and is even larger at lower temperatures. If we compare this value with the H₂ number densities shown in Figure 3, we see that most of the molecular gas in our simulations is indeed in this effectively optically thin regime.

Our results show that a significant fraction of the diffuse [C II] emission produced in the Milky Way simulation is produced by the CO-dark molecular gas component. However, this only accounts for around half of the total diffuse emission, with the remaining half coming from regions dominated by atomic gas. Separating these two contributions – essential if we are to use the [C II] emission as a tracer of the CO-dark gas – is unlikely to be straightforward. In addition, the emissivity per unit mass changes significantly over the range of densities and temperatures occupied by the CO-dark gas. As a result, the relationship between the [C II] surface brightness and the H₂ column density is not linear, as illustrated in Figure 9. For lines-of-sight with $N_{\text{H}_2} < 10^{21} \text{ cm}^{-2}$, corresponding to visual extinctions below $A_V \sim 1$, the [C II] surface brightness scales with N_{H_2} approx-

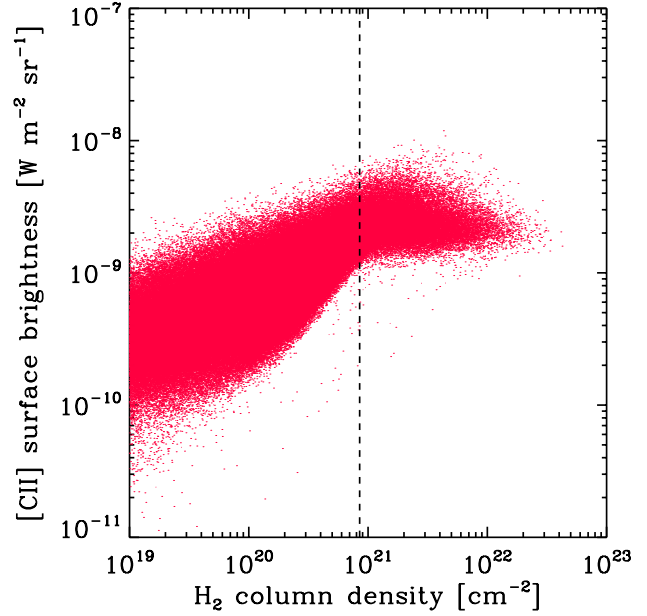


Figure 9. Estimated [C II] surface brightness, plotted as a function of the H₂ column density, for the Milky Way simulation at time $t = 261.1 \text{ Myr}$. The vertical dashed line indicates the H₂ column density at which we would expect the [C II] line to become optically thick, computed assuming a [C II] 1D velocity dispersion $\sigma_{1\text{D}} = 1 \text{ km s}^{-1}$ (see Appendix A). For larger linewidths, this column density scales as $N \propto \sigma_{1\text{D}}$. Note that as our calculation of the [C II] surface brightness does not account for the line opacity, the flattening that we see in the relationship between $I_{\text{C II}}$ and N_{H_2} is not an optical depth effect. Rather, it is a chemical effect: at higher N_{H_2} , most of the carbon is in the form of CO, and so we just see a constant [C II] surface brightness coming from the “skin” of the cloud.

imately as $I_{\text{C II}} \propto N_{\text{H}_2}^{1/2}$, although the scatter around this relationship is considerable. At higher H₂ column densities, however, this relationship breaks down. In this regime, we are probing dense, CO-bright clouds, and so increasing the H₂ column density merely increases the CO column density, but does not significantly affect the amount of C⁺ along the line-of-sight. We therefore find that at high N_{H_2} , the [C II] surface brightness becomes approximately constant. Essentially, what we are seeing is the emission from the C⁺-rich “skin” of the dense molecular cloud.

A further problem with using [C II] emission to trace CO-dark molecular gas in the ISM conditions modelled in our Milky Way simulation concerns the detectability of the resulting emission. In Figure 10, we show a map of the [C II] surface brightness as seen by an observer looking straight down onto the disk. We see that even in the brightest regions, the [C II] surface brightness does not exceed $1.2 \times 10^{-8} \text{ W m}^{-2} \text{ sr}^{-1}$, and that much of the CO-dark H₂ is traced by emission with a [C II] surface brightness of only a few times $10^{-9} \text{ W m}^{-2} \text{ sr}^{-1}$. For comparison, maps of [C II] emission from nearby spiral galaxies made using the PACS instrument on board the *Herschel* satellite typically have 3σ detection thresholds of around a few times $10^{-9} \text{ W m}^{-2} \text{ sr}^{-1}$ to $10^{-8} \text{ W m}^{-2} \text{ sr}^{-1}$ (Croxall et al. 2012; Parkin et al. 2013). With the FIFI-LS instrument on board the SOFIA observa-

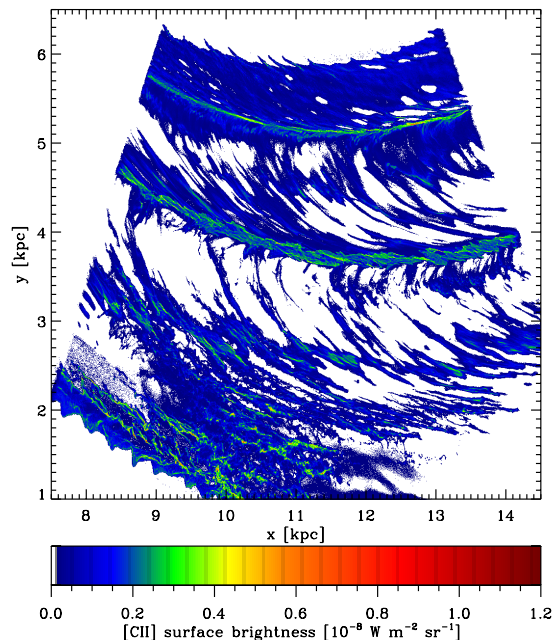


Figure 10. Map of the estimated [C II] surface brightness in our Milky Way simulation at time $t = 261.1$ Myr. Regions shown in white have surface brightnesses $I_{\text{CII}} \leq 10^{-10} \text{ W m}^{-2} \text{ sr}^{-1}$.

tory, it may be possible to go slightly deeper in large-scale maps, to around $10^{-9} \text{ W m}^{-2} \text{ sr}^{-1}$ (J. Pineda, private communication). Therefore, we predict that it should be possible to trace the CO-dark H_2 in galaxies similar to the Milky Way using large-scale [C II] maps, but that doing so at high accuracy will be challenging.

If [C II] is a problematic tracer of CO-dark molecular gas in Milky Way-like conditions, then what about [O I]? In this case, the greater energy required to excite the fine structure lines makes [O I] a much worse tracer of the CO-dark molecular component than [C II]. This is illustrated clearly in Figure 11, where we show the density distribution of the estimated [O I] emissivity in the $63 \mu\text{m}$ and $145 \mu\text{m}$ lines. In both cases, the majority of the emission comes from gas with $T > 100 \text{ K}$, which we already know is mostly atomic. Only 31.4% of the total emission in the $63 \mu\text{m}$ line comes from H_2 -dominated gas and consequently the correlation between the surface brightness of this line and the H_2 column density is almost non-existent (Figure 12). For the $145 \mu\text{m}$ line of [O I], the situation is very similar: only 30.8% of the total emission is produced by H_2 -dominated regions, and there is no correlation between the surface brightness of the line and the H_2 column density.

5.2.2 Results from the other simulations

We have also investigated the behaviour of the [C II] and [O I] emissivities within our other three simulations. However, we find that in the Low and Weak simulation, the [C II] and [O I] emission is extremely weak, on account of the low gas temperature, and is unlikely to be detectable with current instrumentation. We therefore do not examine the distribution of the emission in this simulation in any detail, and focus our attention on the remaining two simulations.

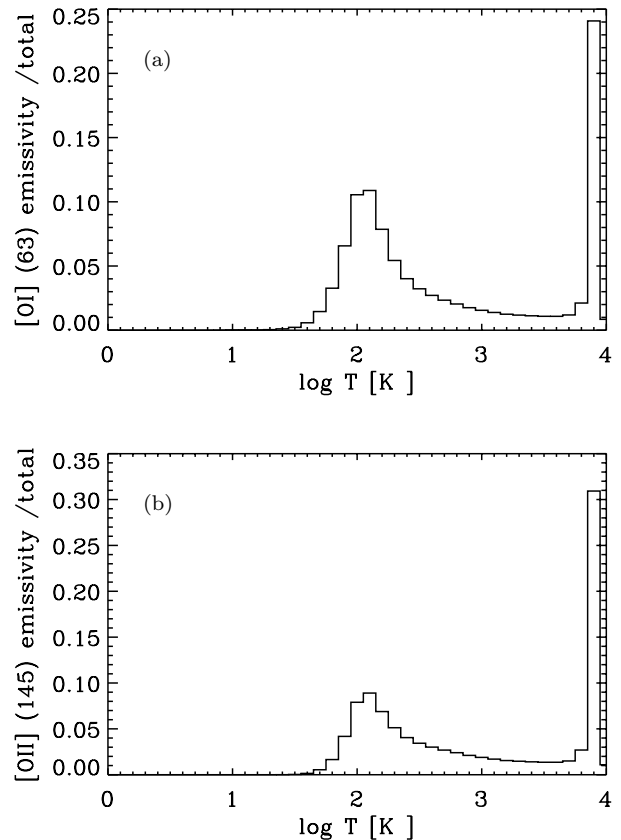


Figure 11. (a) Distribution of the estimated [O I] $63 \mu\text{m}$ emissivity as a function of the gas temperature in our Milky Way simulation at time $t = 261.1$ Myr. (b) As (a), but for the $145 \mu\text{m}$ line of [O I].

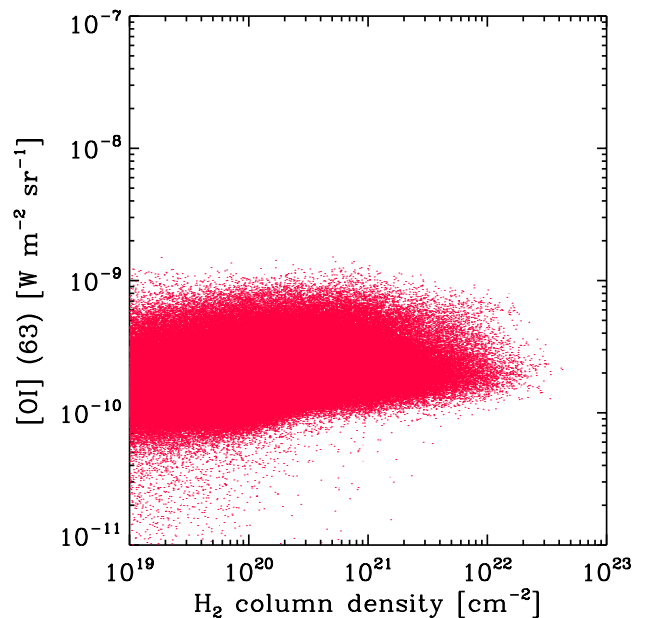


Figure 12. As Figure 9, but for the [O I] $63 \mu\text{m}$ line.

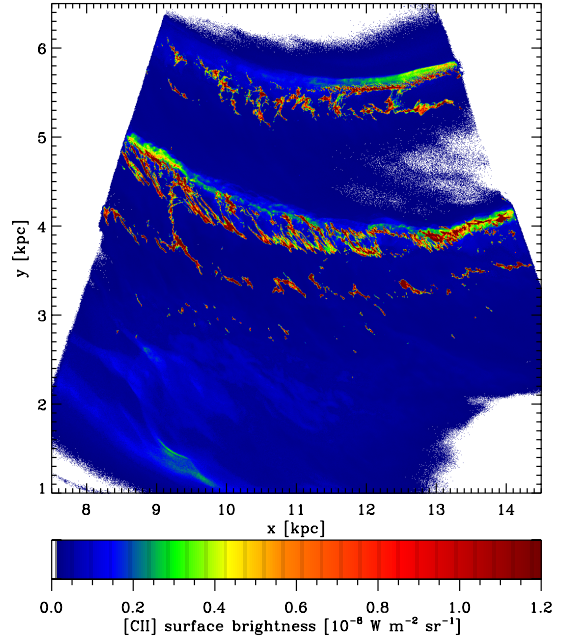
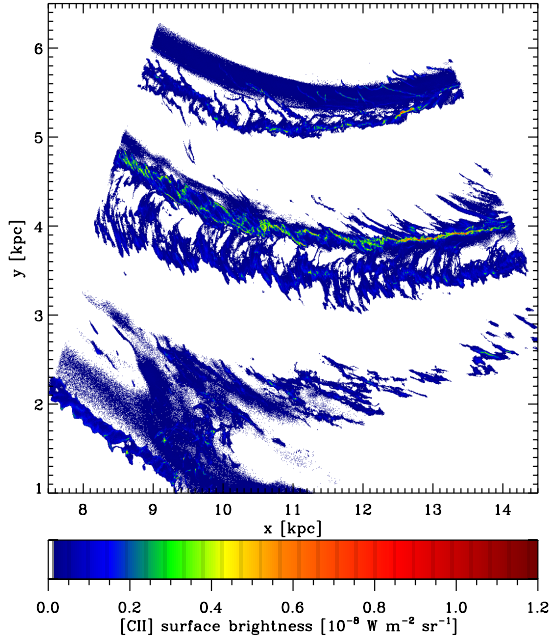


Figure 13. As Figure 10, but for the Low Density simulation.

In Figure 13, we show a map of the [C II] surface brightness in our Low Density simulation at $t = 261.1$ Myr. Comparing this with Figure 10, we see immediately that although the strength of the [C II] emission from the spiral arms is roughly comparable to that in the spiral arms in the Milky Way simulation, the [C II] surface brightness from the inter-arm regions is much lower and is unlikely to be detectable. The temperature and chemical composition of the gas in the inter-arm regions is comparable in both simulations, and so the difference in [C II] surface brightness is driven primarily by the difference in the surface density of the gas in these regions in the two simulations. Specifically, we found already in Smith et al. (2014) that much less dense structure formed in the inter-arm regions in the Low Density simulation than in the Milky Way simulation. This led to a large difference in the CO brightness of these two regions, and we see here that it also strongly affects the [C II] surface brightness of the inter-arm gas. We see similar behaviour if we look at the spatial distribution of the [C II] surface brightness in the Strong Field simulation (Figure 14). Again, there is less dense structure in the inter-arm regions than in the Milky Way run, and this is reflected in the [C II] emission map. However, we also see that in the regions where there is significant emission, the [C II] surface brightness is much larger. This is a consequence of the higher temperature of the CO-dark H_2 and dense atomic hydrogen in this run, due to the greater photoelectric heating rate. It suggests that it will be much easier to detect [C II] emission from this gas in galaxies that have stronger ISRFs than is typical in the local region of the Milky Way.

The impact of a factor of ten increase in the strength of the ISRF on the [C II] surface brightness becomes even more clear if we examine the correlation between [C II] surface brightness and H_2 column density in the Strong Field run (Figure 15). We see that I_{CII} scales approximately as $I_{\text{CII}} \propto$

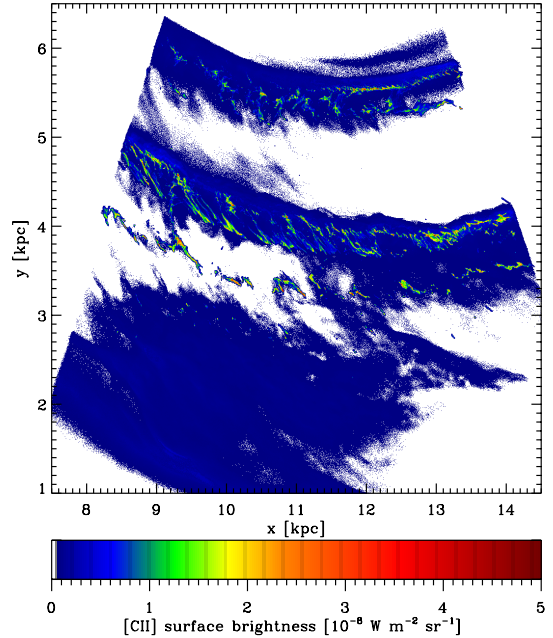


Figure 14. *Top panel:* As Figure 10, but for the Strong Field simulation. The scaling of the colour bar here is the same as in Figure 10, which allows the emission from the diffuse inter-arm gas to be clearly seen, but leads to saturation in the brightest regions of the image. *Bottom panel:* A version of the same figure with a rescaled colour bar that better represents the behaviour of I_{CII} in the brightest regions.

$N_{\text{H}_2}^{1/2}$, just as in the Milky Way run. However, if we compare this figure with Figure 9, we see that at any given H_2 column density, the [C II] surface brightness in the Strong Field run is a factor of five to ten larger than in the Milky Way run. This behaviour is easy to understand from an energetics perspective: an increase in the strength of the ISRF by a factor of ten leads to approximately a factor of ten increase

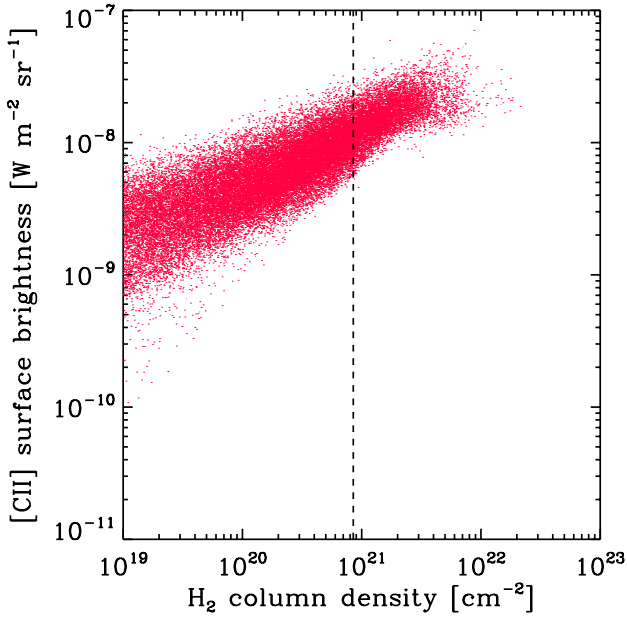


Figure 15. As Figure 9, but for the Strong Field simulation.

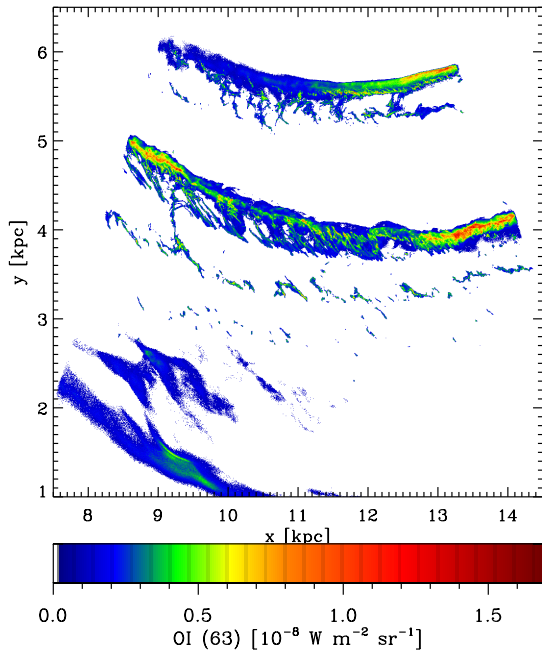


Figure 16. Map of the estimated [O I] 63 μm surface brightness in the Strong Field simulation at time $t = 261.1$ Myr. Regions shown in white have surface brightnesses $I_{\text{OI}} \leq 10^{-9} \text{ W m}^{-2} \text{ sr}^{-1}$.

in the photoelectric heating rate. Therefore, in conditions where [C II] dominates the cooling, we should expect the [C II] luminosity to also increase by approximately an order of magnitude.

Turning to [O I], we start by noting that in the Low Density simulation, the 63 μm line is relatively weak: $I_{\text{OI}} < 10^{-9} \text{ W m}^{-2} \text{ sr}^{-1}$ throughout most of the disk, and hence is

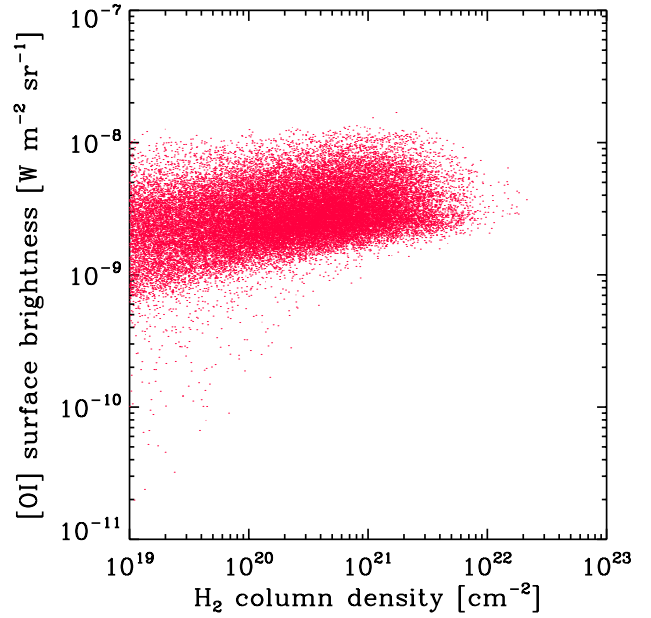


Figure 17. Estimated [O I] 63 μm surface brightness, plotted as a function of the H_2 column density, for the Strong Field simulation at time $t = 261.1$ Myr.

likely undetectable with current instruments. The only region in which we find a higher [O I] surface brightness is in the dense spiral arm in the middle of the high-resolution section of the disk. However, even here I_{OI} never exceeds a few times $10^{-9} \text{ W m}^{-2} \text{ sr}^{-1}$ and the [O I] to [C II] ratio, $I_{\text{OI}}/I_{\text{CII}}$, is much smaller than one. In the Strong Field simulation, on the other hand, the higher gas temperatures lead to significantly higher [O I] surface brightnesses in the spiral arms, as illustrated in Figure 16. However, the correlation between the [O I] surface brightness and the H_2 column density remains very poor (Figure 17), and so even in these warmer conditions, [O I] emission is not a good tracer of CO-dark H_2 .

6 DISCUSSION

6.1 The temperature distribution of CO-dark molecular gas

Our simulations demonstrate that the temperature distribution of CO-dark molecular gas is significantly different from the temperature distribution of the molecular gas that is well-traced by CO emission. CO-bright molecular gas has a low mean temperature, which can be as low as 10 K or as high as 30 K, depending on the strength of the ambient ISRF, and also has a narrow temperature distribution. CO-dark molecular gas, on the other hand, has a much higher mean temperature, ranging from 74 K in the Low and Weak simulation to 105 K in the Strong Field simulations. The CO-dark H_2 also occupies a broader range of temperatures than the CO-rich gas. It is clear from this that temperatures derived using molecular tracers (e.g. CO itself or NH_3) are only useful for describing the behaviour of the CO-bright

gas, and not for constraining the temperature of the CO-faint material.

In addition, if we compare the temperature distribution of the cold H I in our simulations with that of the CO-dark H₂, we see that although there are more similarities, the two temperature distributions are not the same. H I is typically found in slightly warmer gas than CO-dark H₂, since the conditions that favour H₂ formation (higher densities, moderate amounts of shielding) also allow the gas to reach lower temperatures than the lower density gas dominated by atomic hydrogen. Therefore, temperature measurements made using H I emission or absorption are also only of limited usefulness in constraining the temperature of the CO-dark H₂.

One consequence of this is that the sound speed of the CO-dark molecular gas is significantly lower than that of the cold H I. If we compute the mass-weighted mean sound speed of the regions dominated by cold H I in our Milky Way simulation (i.e. regions with molecular fractions of less than 50% and temperatures $T < 300$ K), then we find that $c_{s,\text{CNM}} = 1.15 \text{ km s}^{-1}$. This value is only weakly dependent on the value we take for the upper limit on T , provided that it is higher than a few hundred K. For comparison, the mass-weighted mean sound speed of the H₂-dominated regions (i.e. those with molecular fractions greater than 50%) is $c_{s,\text{H}_2} = 0.47 \text{ km s}^{-1}$ if we consider all of the H₂-dominated regions, increasing to $c_{s,\text{dark}} = 0.64 \text{ km s}^{-1}$ if we only include cells in which less than 1% of the total carbon is locked up in CO.

This difference in sound speeds has two important consequences. First, it implies that the Jeans mass in the CO-dark molecular gas will generally be smaller than in the H I-dominated regions, meaning that the molecular regions will be more unstable to gravitational collapse. Second, if the turbulent velocity dispersion in the H I-dominated gas is similar to that in the CO-dark H₂, then turbulence will have an easier job creating dense structures in the latter than in the former. For example, we know that for an isothermal, supersonically turbulent gas, the logarithmic density variance scales as (Molina et al. 2012)

$$\sigma^2 = \ln \left[1 + b^2 \left(\frac{\beta}{\beta + 1} \right) \mathcal{M}^2 \right], \quad (7)$$

where $\mathcal{M} \equiv \sigma_v/c_s$ is the Mach number of the turbulence, β is the ratio of the thermal pressure to the magnetic pressure, given by $\beta \equiv 2c_s^2/v_A^2$ where v_A is the Alfvén velocity, and b is a parameter that depends on the nature of the turbulent forcing (Federrath et al. 2008, 2010). In a non-isothermal gas, one recovers a slightly different relationship between σ and \mathcal{M} (Nolan, Federrath & Sutherland 2015), but the general point that an increase in \mathcal{M} leads to an increase in the density variance (i.e. an increased number of highly over-dense or under-dense regions) remains valid. Together, these factors mean that it is easier to form gravitationally bound clouds in regions of CO-dark molecular gas than in regions of cold atomic gas. It also implies that simulations of cloud formation in the ISM that do not account for the transition from H I to H₂ will tend to underestimate the formation rate of gravitationally bound clouds.

Another important implication of the fact that the CO-dark H₂ has a relatively broad temperature distribution concerns its detectability using the fine structure lines of [C II]

and [O I]. The excitation rate of [C II] due to collisions with H₂ increases by a factor of ten as we increase the temperature from 30 K to 100 K, and so the warmer the H₂, the easier it is to trace using [C II] emission. Consequently, attempts to map the distribution of CO-dark molecular gas using [C II] emission (e.g. Langer et al. 2014) inevitably give us a somewhat biased picture, as they preferentially pick out warmer gas and may not have sufficient sensitivity to detect CO-dark H₂ in relatively cold regions. In the case of [O I], the excitation rate changes by an even larger factor over the temperature range $30 < T < 100$ K, and so the bias is even greater.

6.2 Caveats

As previously discussed in Smith et al. (2014), there are several caveats that should be taken into account when considering the results of our simulations. First, and most importantly, there is the fact that in the simulations discussed here, we do not account for the effects of either self-gravity or stellar feedback. Although we expect the effects of these processes to cancel out to some extent, with stellar feedback disrupting clouds that would otherwise undergo runaway gravitational collapse, our neglect of both processes nonetheless represents a major simplification in comparison to the real ISM. Note, however, that we would expect both processes to have a much stronger impact on the behaviour of the relatively dense, CO-rich molecular gas than on the comparatively diffuse CO-dark H₂.

A second important simplification in our models is our assumption of a uniform interstellar radiation field. On small scales (e.g. close to regions of massive star formation), this assumption clearly breaks down, but on large scales it should be a reasonable approximation (Wolfire et al. 2003). Our assumption of a constant metallicity and a constant dust-to-gas ratio also represents a simplification in comparison to the real Milky Way, which has a slight metallicity gradient (see e.g. Luck et al. 2011), although for the range of radii we simulate, this corresponds to a change in metallicity of less than a factor of two.

Finally, the treatment of CO chemistry used in these simulations (based on Nelson & Langer 1997) is somewhat approximate and is known to over-produce CO in turbulent clouds in comparison to more sophisticated models (Glover & Clark 2012a). Consequently, we may mis-classify as CO-rich some gas that should actually be CO-dark. However, accounting for this will only broaden the temperature distribution of the CO-dark H₂, strengthening our main conclusions.

7 SUMMARY

We have investigated the temperature distribution of molecular gas in a set of simulations of a representative portion of the ISM of a disk galaxy. Our simulations were carried out using the AREPO moving-mesh code and include a treatment of the non-equilibrium chemistry and thermal evolution of the gas in the ISM. For simplicity, in our current simulations we do not account for the effects of self-gravity, star formation or stellar feedback, but we do account for the influence of the large-scale interstellar radiation field.

In our fiducial run, which has a surface density and ISRF strength characteristic of the local ISM, we find that there is a clear difference between the temperature distribution of CO-bright and CO-dark molecular gas. CO-bright regions have a narrow distribution of temperatures, $10 < T < 30$ K, in good agreement with observational estimates of temperatures in Galactic GMCs. However, the temperature distribution of the CO-dark gas is much broader, covering the range $10 < T < 100$ K. This temperature range overlaps with the range of temperatures that we find in regions dominated by cold atomic hydrogen, but the two temperature distributions are not the same: the CO-dark molecular gas is colder, on average, than the atomic gas. This implies that the temperatures that we can infer from H I observations of cold atomic gas are not a reliable proxy for the temperatures in the CO-dark gas. An important consequence of this is the fact that the mean sound speed of the CO-dark molecular component is significantly smaller than that of the cold atomic gas, differing by almost a factor of two in our fiducial run. As a result, the molecular component will be more susceptible to turbulent compression and gravitational collapse than the atomic gas, implying that the chemical transition from H to H₂ can help to promote star formation even though the H₂ molecules themselves play no role in cooling the gas at these temperatures (Glover & Clark 2012c).

We have explored how these results vary as we vary the initial surface density of the gas and the strength of the ISRF. Decreasing the surface density while keeping the ISRF strength fixed leads to a large change in the temperature distribution of the molecular gas, owing to the substantially decreased effectiveness of shielding in this case. The CO-bright gas almost entirely vanishes (c.f. Smith et al. 2014) and the temperature distribution of the H₂ changes from being relatively flat between 10 K and 100 K to being sharply peaked around 100 K. On the other hand, if we decrease the strength of the ISRF at the same time as we decrease the surface density, we find that we retain the cold H₂. Indeed, in this case, there is significantly more H₂ with $T \sim 20$ –30 K and significantly less with $T \sim 100$ K than in our fiducial run, despite the lower surface density. Finally, if we keep the surface density of the gas fixed and increase the strength of the ISRF, we find that the temperature distribution of the H₂ again becomes strongly peaked around $T \sim 100$ K. However, in this case, unlike in the low surface density run, we retain a significant amount of relatively cold H₂.

We have also investigated the potential detectability of the CO-dark H₂ using the [C II] and [O I] fine structure lines. The wide range of spatial scales covered by our simulations means that it is impractical to post-process them using a radiative transfer code in order to compute the integrated intensities of the lines without substantial smoothing. We have therefore estimated the line strengths using a simple approach that does not require us to smooth the data. The main approximation made in this approach is the assumption that the lines remain optically thin, which is valid for low column density lines of sight but causes us to overestimate the emission for lines of sight with $A_V > 1$.

In our fiducial simulation, we find that roughly equal amount of emission are produced in regions dominated by atomic hydrogen and in regions dominated by CO-dark H₂. In the latter regions, the typical [C II] surface

brightness ranges from a few times 10^{-9} W m⁻² sr⁻¹ up to 10^{-8} W m⁻² sr⁻¹. Although faint, this is in principle detectable with modern instruments such as FIFI-LS, albeit with relatively low signal-to-noise. However, even if detected, interpreting this emission may be difficult: distinguishing between emission from regions dominated by atomic hydrogen and those dominated by CO-dark H₂ may not be straightforward and there is only a weak correlation between the [C II] surface brightness and the H₂ column density. For the [O I] lines, the situation is less promising: both lines are significantly fainter and there is essentially no correlation between their surface brightness and the H₂ column density.

Comparing the results from our fiducial simulation to those from our other simulations, we find that the most important parameter controlling the detectability of the CO-dark molecular gas with the [C II] and [O I] lines is the strength of the ISRF. Increasing the strength of the ISRF increases the photoelectric heating rate and hence the temperature of the CO-dark molecular gas, causing it to emit more strongly in [C II] and [O I]. Conversely, decreasing the strength of the ISRF makes this gas colder and hence much harder to map using these lines. We also find that even in the most favourable conditions for detecting [C II] and [O I], their usefulness as a tracer of CO-dark H₂ is questionable: [C II] emission is only weakly correlated with H₂ column density, and [O I] emission is almost completely uncorrelated with H₂.

ACKNOWLEDGEMENTS

The authors would like to thank P. Clark, R. S. Klessen, J. Pineda and V. Springel for useful discussions. They would also like to thank the anonymous referee for their comments on a earlier draft of this paper. SCOG acknowledges financial support from the Deutsche Forschungsgemeinschaft (DFG) via SFB 881 “The Milky Way System” (subprojects B1, B2 and B8) and via SPP 1573 “Physics of the Interstellar Medium” (grant number GL 668/2-1). RJS gratefully acknowledges support from the Royal Astronomical Society through their Norman Lockyer Fellowship. The numerical simulations described in this paper were performed on the Milky Way supercomputer, which is funded by the DFG through SFB 881 (subproject Z2) and hosted and co-funded by the Jülich Supercomputing Center (JSC).

REFERENCES

- Abrahamsson, E., Krems, R. V., & Dalgarno, A. 2007, *ApJ*, 654, 1171
- Allen, R. J., Ivette Rodríguez, M., Black, J. H., & Booth, R. S. 2012, *AJ*, 143, 97
- Bell, K. L., Berrington, K. A., & Thomas, M. R. J. 1998, *MNRAS*, 293, L83
- Bertram, E., Glover, S. C. O., Clark, P. C., & Klessen, R. S. 2015, *MNRAS*, 451, 3679
- Binney, J., & Tremaine, S. 1987, *Galactic Dynamics*, (Princeton: Princeton University Press)
- Bisbas, T. G., Bell, T. A., Viti, S., Yates, J., & Barlow, M. J. 2012, *MNRAS*, 427, 2100

- Caldwell, J. A. R., & Ostriker, J. P. 1981, *ApJ*, 251, 61
- Clark, P. C., Glover, S. C. O., & Klessen, R. S. 2012, *MNRAS*, 420, 745
- Clark, P. C., Glover, S. C. O., Klessen, R. S., & Bonnell, I. A. 2012, *MNRAS*, 424, 2599
- Croxall, K. V., et al. 2012, *ApJ*, 747, 81
- Cox, D. P., & Gómez, G. C. 2002, *ApJS*, 142, 261
- Dobbs, C. L., Bonnell, I. A., & Pringle, J. E. 2006, *MNRAS*, 371, 1663
- Draine, B. T., 1978, *ApJS*, 36, 595
- Draine, B. T., & Bertoldi, F. 1996, *ApJ*, 468, 269
- Federrath, C., Klessen, R. S., & Schmidt, W. 2008, *ApJ*, 688, L79
- Federrath, C., Roman-Duval, J., Klessen, R. S., Schmidt, W., & Mac Low, M.-M. 2010, *A&A*, 512, A81
- Gent, F. A., Shukurov, A., Fletcher, A., Sarson, G. R., & Mantere, M. J. 2013, *MNRAS*, 432, 1396
- Girichidis, P., et al. 2016, *MNRAS*, 456, 3432
- Glover, S. C. O., & Mac Low, M.-M. 2007a, *ApJS*, 169, 239
- Glover, S. C. O., & Mac Low, M.-M. 2007b, *ApJ*, 659, 1317
- Glover, S. C. O., Federrath, C., Mac Low, M.-M., & Klessen, R. S. 2010, *MNRAS*, 404, 2
- Glover, S. C. O., & Clark, P. C. 2012a, *MNRAS*, 421, 116
- Glover, S. C. O., & Clark, P. C. 2012b, *MNRAS*, 426, 377
- Glover, S. C. O., & Clark, P. C. 2012c, *MNRAS*, 421, 9
- Glover, S. C. O., Clark, P. C., Micic, M., & Molina, F. 2015, *MNRAS*, 448, 1607
- Goldsmith, P. F., Langer, W. D., Pineda, J. L., & Velusamy, T. 2012, *ApJS*, 203, 13
- Górski, K. M., Hivon, E., Banday, A. J., Wandelt, B. D., Hansen, F. K., Reinecke, M., & Bartelmann, M. 2005, *ApJ*, 622, 759
- Greif, T. H., Springel, V., White, S. D. M., Glover, S. C. O., Clark, P. C., Smith, R. J., Klessen, R. S., & Bromm, V. 2011, *ApJ*, 737, 75
- Greif, T. H., Bromm, V., Clark, P. C., Glover, S. C. O., Smith, R. J., Klessen, R. S., Yoshida, N., & Springel, V. 2012, *MNRAS*, 424, 399
- Grenier, I. A., Casandjian, J.-M., Terrier, R. 2005, *Science*, 307, 1292
- Hennebelle, P., & Iffrig, O. 2014, *A&A*, 570, A81
- Hill, A. S., Joung, M. R., Mac Low, M.-M., Benjamin, R. A., Haffner, L. M., Klingenberg, C., & Waagan, K. 2012, *ApJ*, 750, 104
- Hollenbach, D. J., & McKee, C. F. 1989, *ApJ*, 342, 306
- Hughes, A., Meidt, S. E., Colombo, D., Schinnerer, E., Pety, J., Leroy, A. K., Dobbs, C. L., García-Burillo, S., Thompson, T. A., & Dumas, G. 2013, *ApJ*, 779, 46
- Jackson, J. M., Rathborne, J. M., Shah, R. Y., Simon, R., Bania, T. M., Clemens, D. P., Chambers, E. T., Johnson, A. M., Dormody, M., Lavoie, R., & Heyer, M. H. 2006, *ApJS*, 163, 145
- Jaquet, R., Staemmler, V., Smith, M. D., & Flower, D. R. 1992, *J. Phys. B*, 25, 285
- Krumholz, M. R., McKee, C. F., & Tumlinson, J. 2008, *ApJ*, 689, 865
- Langer, W. D., Velusamy, T., Pineda, J. L., Willacy, K., & Goldsmith, P. F. 2014, *A&A*, 561, 122
- Lee, H.-H., Herbst, E., Pineau des Forêts, G., Roueff, E., & Le Bourlot, J. 1996, *A&A*, 311, 690
- Luck, R. E., Andrievsky, S. M., Kovtyukh, V. V., Gieren, W., Graczyk, D. 2011, *AJ*, 142, 51
- Maíz-Apellániz, J. 2001, *AJ*, 121, 2737
- Mathis, J. S., Mezger, P.G., & Panagia, N. 1983, *A&A*, 128, 212
- Molina, F. Z., Glover, S. C. O., Federrath, C., & Klessen, R. S. 2012, *MNRAS*, 423, 2680
- Nelson, R. P., & Langer, W. D. 1997, *ApJ*, 482, 796
- Nolan, C. A., Federrath, C., & Sutherland, R. S. 2015, *MNRAS*, 451, 1380
- Nishimura, A., et al., 2015, *ApJS*, 216, 18
- Offner, S. S. R., Bisbas, T. G., Viti, S., & Bell, T. A. 2013, *ApJ*, 770, 49
- Padoan, P., Nordlund, A., & Jones, B. J. T. 1997, *MNRAS*, 288, 145
- Paradis, D., Dobashi, K., Shimoikura, T., Kawamura, A., Onishi, T., Fukui, Y., & Bernard, J.-P. 2012, *A&A*, 543, 103
- Parkin, T. J., et al. 2013, *ApJ*, 776, 65
- Parravano, A., Hollenbach, D. J., & McKee, C. F. 2003, *ApJ*, 584, 797
- Pequignot, D. 1990, *A&A*, 231, 499
- Polychroni, D., Moore, T. J. T., & Allsopp, J. 2012, *MNRAS*, 422, 2992
- Rachford, B. L. 2009, *ApJS*, 180, 125
- Reed, B. C. 2000, *AJ*, 120, 314
- Reipurth, B., & Bally, J. 2001, *ARA&A*, 39, 403
- Roman-Duval, J., Jackson, J. M., Heyer, M., Rathborne, J., & Simon, R. 2010, *ApJ*, 723, 492
- Schöier, F. L., van der Tak, F. F. S., van Dishoeck, E. F., & Black, J. H. 2005, *A&A*, 432, 369
- Sembach, K. R., Howk, J. C., Ryans, R. S. I., & Keenan, F. P. 2000, *ApJ*, 528, 310
- Shaw, G., Ferland, G. J., Srianand, R., & Abel, N. P. 2006, *ApJ*, 639, 941
- Smith, R. J., Shetty, R., Beuther, H., Klessen, R. S., & Bonnell, I. A. 2013, *ApJ*, 771, 24
- Smith, R. J., Glover, S. C. O., Clark, P. C., Klessen, R. S., & Springel, V. 2014, *MNRAS*, 441, 1628
- Snow, T. P., & McCall, B. J. 2006, *ARA&A*, 44, 367
- Springel, V. 2010, *MNRAS*, 401, 791
- Stancil, P. C., Schultz, D. R., Kimura, M., Gu, J.-P., Hirsch, G., & Bunker, R. J. 1999, *A&AS*, 140, 225
- Sternberg, A., Le Petit, F., Roueff, E., & Le Bourlot, J. 2014, *ApJ*, 790, 10
- Tielens, A. G. G. M., & Hollenbach, D. 1985, *ApJ*, 291, 722
- van Dishoeck, E. F., & Black, J. H. 1988, *ApJ*, 334, 771
- van der Tak, F. F. S., & van Dishoeck, E. F., *A&A*, 358, L79
- Velusamy, T., & Langer, W. D. 2014, *A&A*, 572, A45
- Walch, S., et al. 2015, *MNRAS*, 454, 246
- Wiesenfeld, L., & Goldsmith, P. F. 2014, *ApJ*, 780, 183
- Wilson, N. J., & Bell, K. L. 2002, *MNRAS*, 337, 1027
- Wolfire, M. G., McKee, C. F., Hollenbach, D., & Tielens, A. G. G. M. 2003, *ApJ*, 587, 278
- Wolfire, M. G., Hollenbach, D., & McKee, C. F. 2010, *ApJ*, 716, 1191

APPENDIX A: WHEN DO THE [C II] AND [O I] LINES BECOME OPTICALLY THICK?

We can assess the conditions in which the optically thin approximation for treating [C II] and [O I] emission is valid by computing the column density of ground state C^+ ions or oxygen atoms needed to produce an optical depth $\tau = 1$ in the $158 \mu\text{m}$ or $63 \mu\text{m}$ lines, respectively. For the purposes of this calculation, we conservatively assume that the broadening of both lines is dominated by turbulent motions with a one-dimensional velocity dispersion of $\sigma_{1D} = 1 \text{ km s}^{-1}$. In practice, it is likely that in many of the CO-dark regions, σ_{1D} will be higher than this, meaning that the required column densities will be larger.

We find that with this assumption, the [C II] $158 \mu\text{m}$ line becomes optically thick once the C^+ column density exceeds $N_{C^+} \simeq 2.4 \times 10^{17} \text{ cm}^{-2}$. If all of the carbon along the line-of-sight is in the form of C^+ , then this corresponds to a total hydrogen column density $N_{H,\text{tot}} = N_{C^+}/x_{C,\text{tot}} \simeq 1.7 \times 10^{21} \text{ cm}^{-2}$, or a visual extinction of $A_V \sim 1$. This is close to the point at which carbon starts to become locked up in CO in our simulations, and implies that by assuming optically thin emission, we may overestimate the emission coming from ionized carbon gas in the immediate vicinity of GMCs, but will probably not significantly overestimate the emission coming from more diffuse regions. For the [O I] $63 \mu\text{m}$ line, the column density of atomic oxygen required to produce an optically thick line is somewhat larger, $N_O \simeq 6 \times 10^{17} \text{ cm}^{-2}$. However, the total oxygen abundance in the ISM is also larger, and so we expect the line to become optically thick at roughly the same hydrogen column density. Therefore, the same caveats apply as in the case of [C II].

Note also that in both cases, if the emission is produced primarily in gas with a density much less than the critical density of the transition, then the line can be effectively thin even if $\tau > 1$. In this regime, discussed in more detail in Goldsmith et al. (2012) for the case of [C II], the photons are absorbed and re-emitted multiple times, but the fraction of the radiated energy that is converted back into heat by collisional de-excitation of excited C^+ or O remains very small.

Finally, we note that as the density of the gas in our simulations is everywhere much smaller than the critical density of [O I], $n_{\text{crit}} \simeq 10^6 \text{ cm}^{-3}$, we would not expect the [O I] $145 \mu\text{m}$ line to be optically thick anywhere within our simulations.